Numerical investigation on movement of triple points on oblique detonation surfaces ⓔⓟ

Pengfei Yang (杨鹏飞); Haoyang Li (李昊洋) ✉; Zheng Chen (陈正); ... et. al

Check for updates

CrossMark

View Online

Export Citation

Articles You May Be Interested In

Unsteady dynamics of wedge-induced oblique detonations under periodic inflows
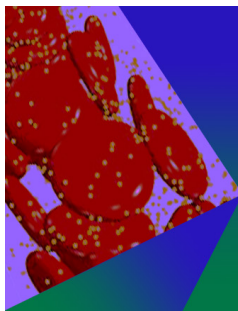
Physics of Fluids (January 2021)

Structure of wedge-induced oblique detonation in acetylene-oxygen-argon mixtures

Physics of Fluids (February 2019)

Numerical investigation of free oblique detonation wave induced by non-intrusive energy deposition

AIP Advances (December 2021)

Physics of Fluids

Special Topic: Flow and Forensics

Submit Today!

AIP Publishing

AIP Publishing

Numerical investigation on movement of triple points on oblique detonation surfaces EP

Pengfei Yang (杨鹏飞),[1] (iD) Haoyang Li (李昊洋),[2,3,a] (iD) Zheng Chen (陈正),[1] (iD) Chun Wang (王春),[2] (iD) and Honghui Teng (滕宏辉)[4] (iD)

AFFILIATIONS

[1]State Key Laboratory for Turbulence and Complex Systems (SKLTCS), Center for Applied Physics and Technology (CAPT), College of Engineering, Peking University, Beijing 100871, China
[2]State Key Laboratory of High Temperature Gas Dynamics, Institute of Mechanics, Chinese Academy of Sciences, Beijing 100190, China
[3]School of Engineering Sciences, University of Chinese Academy of Sciences, Beijing 100049, China
[4]School of Aerospace Engineering, Beijing Institute of Technology, Beijing 100081, China

[a]Author to whom correspondence should be addressed: lihaoyang20@mails.ucas.ac.cn

ABSTRACT

A normal detonation wave in a gaseous mixture is a transient, multidimensional structure containing triple points (TPs) that collide in pairs and then propagate oppositely. However, the TPs on an oblique detonation wave (ODW) almost propagate along the same direction in most studies. In this study, the reactive Euler equations coupled with a two-step induction–reaction kinetic model are used to solve a two-dimensional wedge-induced ODW. Two novel movement patterns are observed in most cases. Results show that the TPs of the ODW can propagate upstream and even stand on the wave surface. The movement patterns of TPs include downstream, upstream, and steady according to their propagation direction relative to the wedge. We find that the ratio of the post-ODW flow speed U_τ to the transverse wave speed U_T dominates the TP movement types. When the speed ratio U_τ/U_T is approximately equal to 1, the TPs can stand on the wave surface. Above unity, downstream TPs form, and upstream TPs correspond to a value smaller than 1. Furthermore, the inflow Mach number has little influence on U_T, while U_τ changes significantly. This is largely due to the high sensitivity of the ODW angle to the inflow. The high heat release rate benefits upstream TPs, and steady TPs form under a large wedge angle. The results are confirmed by varying the inflow Mach number, wedge angle, and chemical parameters.

Published under an exclusive license by AIP Publishing. https://doi.org/10.1063/5.0091078

I. INTRODUCTION

Gaseous detonation is an extreme combustion mode that is triggered by a strongly leading shock. It means that a high thermal efficiency of pressure-gain-combustion can be achieved. Therefore, a detonation wave has an important application prospect in aerospace engineering. Three kinds of engines based on detonation have been proposed and studied widely:[1–6] the rotating detonation engine (RDE), pulse detonation engine (PDE), and oblique detonation engine (ODE).

A detonation wave contains complex shock wave dynamics and chemical reaction processes and has a complex structure. A normal detonation wave (NDW) propagating in a tube was first studied extensively. Many experiments[7–11] have also shown that the TPs propagating along the NDW front form a complex multi-wave structure, which is called a cellular structure. Figure 1(a) displays TP evolution on a propagating cellular NDW. As the detonation wave front advances, two adjacent TPs collide continuously, resulting in alternating changes in the incident wave and the Mach stem. Then, the incident wave evolves into a Mach stem, and the Mach stem evolves into an incident wave. The propagation direction of two adjacent transverse waves also changes. The TP path has strong symmetry along the NDW propagation direction.

The surface of an ODW is similar to that of an NDW because the ODW surface can also be destabilized, which induces a local small-scale wave structure. This has also been confirmed by simulations[12] and experiments.[13] However, the wave surface and incoming flow of the ODW are not perpendicular, which is different from the case of the NDW, and the tangential component of the incoming flow along the ODW wave surface has a strong influence on the movement patterns of TPs. Most TPs on the ODW surface generally propagate downstream,[14–21] as shown in Fig. 1(b).
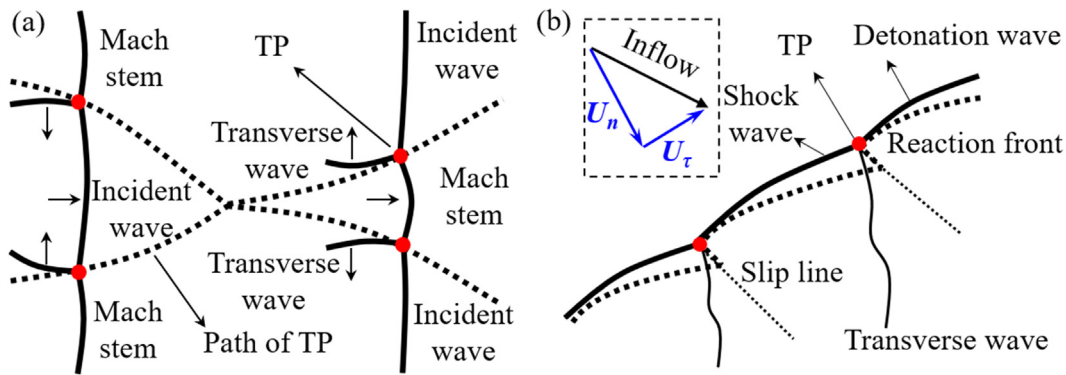
FIG. 1. Evolution of TPs in cellular detonations (a) and diagram of an ODW front with TPs (b).

The structure and propagation patterns of ODW TPs are more complex than those of NDW TPs. Many studies[14–16] have observed two instability processes in ODWs: primary and secondary instabilities. During the primary instability, one set of transverse waves are generated whose own velocity is the opposite of inflow velocity. Therefore, their absolute velocity in laboratory coordinates is the difference between the inflow velocity and their own velocity. Only when the secondary instability occurs, are another set of transverse waves generated whose own velocity is the same as inflow velocity. Therefore, their absolute velocity in laboratory coordinates is the sum of inflow velocity and their own velocity. The absolute velocities of two sets of transverse waves are different, and the difference in velocity causes them to collide with each other. The primary instability generates single-sided TPs, while TPs with a dual-headed structure are generated in the secondary instability. The wave surface also evolves from a "sawtooth" flame front to a "keystone"-shaped flame surface in the transition from the primary to the secondary instability.[17] Studies[18,19] have also found that formation of single-sided TPs not only precedes, but also provides the condition for formation of dual-headed TPs.

Most studies have mostly focused on the instability mechanism of the wave surface and the TP structure. TP propagation patterns, however, have been greatly neglected. The TPs on the wave surface propagate not only downstream, but also sometimes upstream, and have even been observed to stand on the wave surface in a few cases. Choi et al.[22] found that upstream TPs result in instability of the ODW initiation structure. Liu et al.[23] studied the influence of external disturbances on the ODW flow field, where TPs stand on the wave surface. However, what causes the different types of TPs to propagate in different directions is still unknown.

Motivated by the above unsolved problems, this study adopts a two-step chemical kinetic model to analyze the propagation patterns of TPs on the wave surface of an ODW induced by a two-dimensional, semi-infinite wedge. According to the propagation direction relative to the wedge, the TPs generated by the wave surface instability are divided into downstream TPs, upstream TPs, and steady TPs. Inspired by previous research,[24,25] we obtain these types of TPs by adjusting the inflow Mach number M_0, wedge angle θ, and heat release rate k_R, which influence the stability of the ODW surface. Then, we introduce two effect factors, the post-ODW flow speed U_τ and transverse wave velocity U_T, and propose the speed ratio U_τ/U_T as

a dimensionless criterion to explain further the propagation patterns of different TP types.

II. PHYSICAL AND MATHEMATICAL MODEL

Figure 2 is the schematic of a typical ODW induced by a two-dimensional, semi-infinite wedge. In a supersonic reactive inflow, an oblique shock wave (OSW) is first induced by the wedge. The high post-shock temperature behind the OSW induces an exothermic chemical reaction that initiates the ODW. The distance from the apex of the wedge to the beginning of the chemical exothermic reaction along the wedge direction is defined as the length of the initiation zone of the oblique detonation wave L_{ini}. The computational domain is shown by a dashed rectangular box in Fig. 2. The left and upper boundaries are set as the supersonic inflow. Hence, the inflow temperature T, pressure p, and Mach number M_0 are constant. The right outflow is also supersonic, in which the boundary data can be extrapolated from the interior. The lower wedge surface is modeled as a slip wall; hence, the normal gradient of thermodynamic state (T, p, ρ) and the normal velocity on the wall surface is zero. As done in previous studies,[26–30] we assume an inviscid fluid. The ODW flow field is modeled using the reactive Euler equations,

$$\frac{\partial \boldsymbol{U}}{\partial t} + \frac{\partial \boldsymbol{F}}{\partial x} + \frac{\partial \boldsymbol{G}}{\partial y} = \boldsymbol{S}, \tag{1}$$

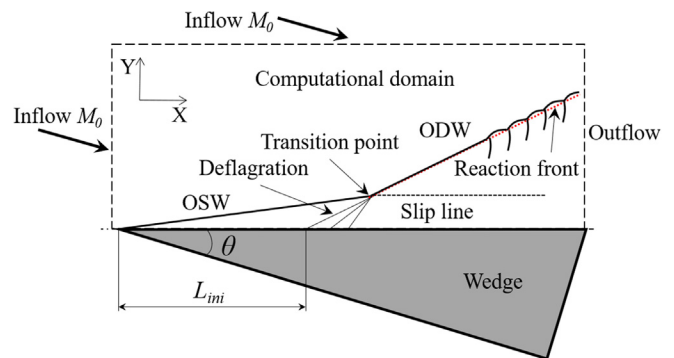**FIG. 2.** Schematic of wedge-induced oblique detonation.

$$U = \begin{Bmatrix} \rho \\ \rho u \\ \rho v \\ \rho e \\ \rho \xi \\ \rho \lambda \end{Bmatrix}, \quad F = \begin{Bmatrix} \rho u \\ \rho u^2 + p \\ \rho uv \\ \rho u(e+p) \\ \rho u \xi \\ \rho u \lambda \end{Bmatrix},$$

$$G = \begin{Bmatrix} \rho v \\ \rho uv \\ \rho v^2 + p \\ \rho v(e+p) \\ \rho v \xi \\ \rho v \lambda \end{Bmatrix}, \quad S = \begin{Bmatrix} 0 \\ 0 \\ 0 \\ 0 \\ \rho \dot{\omega}_1 \\ \rho \dot{\omega}_2 \end{Bmatrix}, \quad (2)$$

with

$$p = \rho T, \quad (3)$$

where the variables ρ, u, v, e, T, and p represent the density, x-velocity, y-velocity, specific total energy, temperature, and pressure, respectively. To make the values more concise and easier to compare, the dimensionless form is adopted in the simulations. All the variables have been nondimensionalized by reference to the uniform unburned state as follows:

$$\rho = \frac{\tilde{\rho}}{\rho_0}, \quad u = \frac{\tilde{u}}{\sqrt{RT_0}}, \quad v = \frac{\tilde{v}}{\sqrt{RT_0}}, \quad p = \frac{\tilde{p}}{p_0}, \quad T = \frac{\tilde{T}}{T_0}. \quad (4)$$

The symbol "$\sim$" denotes original dimensional quantities, and the subscript "0" indicates reference quantities ahead of the detonation/shock front. Therefore, the Mach number is defined as follows:

$$M = \frac{\sqrt{\tilde{u}^2 + \tilde{v}^2}}{\sqrt{\gamma R \tilde{T}}} = \frac{\sqrt{(u^2 + v^2)RT_0}}{\sqrt{\gamma R T_0 T}} = \frac{\sqrt{u^2 + v^2}}{\sqrt{\gamma T}}. \quad (5)$$

The chain-branching kinetics is modeled as a two-step reaction,[31] which is widely used in various detonation simulations.[32–36] Two additional reaction variables are introduced to control the reaction: ξ and λ, which denote the reaction progress variable in the induction period and the chain-recombination reaction progress variable, respectively. Both the value of ξ and λ varies from zero to one. When $\xi < 1$, only the reaction progress in the induction period begins. When $\xi = 1$, the reaction progress in the induction period ends and the chain-recombination reaction progress begin, i.e., $\lambda = 0$. When $\lambda = 1$, the chain-recombination reaction progress ends and the heat is completely released. The reaction rates $\dot{\omega}_1$ and $\dot{\omega}_2$ are given by

$$\dot{\omega}_1 = H(1-\xi)k_I \exp\left[E_I\left(\frac{1}{T_S} - \frac{1}{T}\right)\right], \quad (6)$$

$$\dot{\omega}_2 = [1 - H(1-\xi)](1-\lambda)k_R \exp\left(-\frac{E_R}{T}\right), \quad (7)$$

$$E_I = 4.0T_S, \quad E_R = 1.0T_S, \quad (8)$$

where T_S denotes the post-shock temperature of the one-dimensional Zeldovich–von Neumann–Döring (ZND) detonation. The quantities k_I and k_R are the two key pre-exponential factors. In this study, $k_I = -u_{vn}$, where u_{vn} is the post-shock particle velocity in the

shock-fixed frame for the ZND detonation, with the induction length of the ZND detonation fixed to unity. The factor k_R is the rate constant for the heat release process, which is used as a parameter to control the ratio of the reaction time to the induction time. The Heaviside step function $H(1-\xi)$ is given by

$$H(1-\xi) = \begin{cases} 1, & if \ \xi < 1, \\ 0, & if \ \xi \geq 1. \end{cases} \quad (9)$$

The specific total energy is expressed as

$$e = \frac{p}{\rho(\gamma-1)} + \frac{1}{2}(u^2 + v^2) - \lambda Q, \quad (10)$$

where Q and γ are the nondimensionalized chemical heat release and specific heat ratio, which are fixed to be $Q = \tilde{Q}/(RT_0) = 25$ and $\gamma = 1.2$. This study uses the dispersion-controlled dissipation (DCD) scheme[37] together with a third-order Runge–Kutta algorithm to approximate the solutions of the governing equations. All variables have been scaled by free flow state, as shown in Eq. (4); hence, the dimensionless pressure, temperature, and density of inflow are unity, i.e., $T = 1.0$, $p = 1.0$, and $\rho = 1.0$. For a given state (T_0, p_0, ρ_0) of any reliable mixture, we can obtain the flow parameters through the formula in Eq. (4). The x-velocity u and y-velocity v of inflow are calculated according to M_0 and θ as shown in Fig. 2, and they are $M_0\sqrt{\gamma T_0}\cos\theta$ and $M_0\sqrt{\gamma T_0}\sin\theta$, respectively. The inflow Mach number M_0, wedge angle θ, and heat release rate k_R are set to be variable to get different ODW structures.

III. RESULTS AND DISCUSSION

A. Basic structures of oblique detonation and resolution study

First, the inflow Mach number was set to $M_0 = 6.5$, the wedge angle to $\theta = 30°$, and the heat release rate to $k_R = 1.0$ to simulate the ODW structure. As shown in Fig. 3, we simulated the ODW flow fields with a 0.05×0.05 grid (above) and a 0.025×0.025 grid (below),
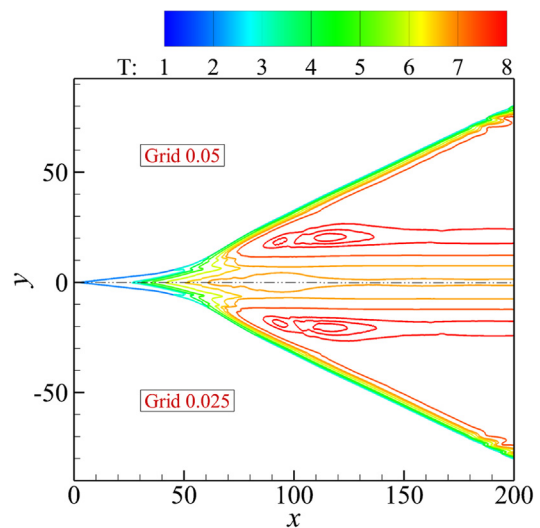

FIG. 3. ODW temperature fields for the basic case: $M_0 = 6.5$, $k_R = 1.0$, and $\theta = 30°$.

which correspond to 20 points and 40 points per unit length of the ZND induction zone. The initiation structure of the ODW in Fig. 3 is characterized by a curved shock, which is considered a smooth transition in other studies.[38–41] For the two grid sizes, the ODWs are both initiated at approximately $x = 50$, where the wave angle obviously increases owing to the heat release. The isotherms are almost the same behind the location of initiation. This study focuses on the instability of the ODW surface, and the location of the ODW instability is an important characteristic. The positions of instability are both approximately at $x = 185$ for the grid sizes 0.05 and 0.025. Adopting the grid size 0.05 satisfies the simulation accuracy required for our study. The chosen chemical parameters, $Q = 25$ and $\gamma = 1.2$, do not correspond to any real reactants, but are rather a generic model with modest heat release and activation energies. This gives a Chapman–Jouguet (CJ) detonation Mach number M_{CJ} of 4.5, which approximately corresponds to the CJ velocity of a hydrocarbon fuel with small molecules and a stoichiometric hydrogen–air mixture (300 K and 100 kPa).

When qualitatively assessing the effect of grid size in Fig. 3, it is difficult to distinguish the differences in the temperature field under the two grid sizes. For a further quantitative comparison, Fig. 4 shows the pressure and temperature profiles along the wedge surface ($y = 0$), the line $y = 20$, and the line $y = 70$, parallel to the x-axis. The line $y = 20$ approximately corresponds to the location of initiation, and the line $y = 70$ corresponds to the location of instability. Along the line $y = 0$, the shock is inert and uncoupled with the heat release reaction, so it results in the long induction region. Nevertheless, for the lines $y = 20$ and $y = 70$, the shock front is strongly coupled with the heat release reaction, which generates a short induction region with a post-shock sharp pressure rise. The pressure peak appears on the surface and then decays rapidly, which differs from the situation on the line $y = 0$. Clearly, the lines $y = 0$ and $y = 20$ overlap for the grid sizes 0.05 and 0.025, and the differences are hardly distinguishable. For $y = 70$, there are acceptable differences for the two grid sizes, which are negligible for the simulation results. In conclusion, the grid size 0.05 guarantees the reliability of the conclusion, so it is used subsequently in this study. To prove the generality of simulated results, many cases under various parameters (inflow Mach number, wedge angle and chemical reaction rate) are solved. Hence, the computational

domains 150×70 and 180×100 are adopted, corresponding to the grid number 3000×1400 and 3600×2000, respectively.

B. Evolution of TPs on ODW surfaces

To get TPs with different movement patterns, we adjusted the chemical reaction parameter k_R and geometrical parameter θ in this section based on the default case in Fig. 3. We used k_R to adjust the structure of the chemical reaction zone and trigger the ODW instability, and θ to affect the wave angle and control the degree of overdrive of the ODW surface. The simulated time of every figure is long enough to guarantee the accuracy of results. Comparing to the simulation of steady initiation zone structure, at least twice as its time was adopted to present the results of wave surface instability.

The effect of the heat release rate k_R was studied first. In Fig. 3, the wave surface instability produces a small-scale wave system at the downstream position. The structure propagates downstream continuously, and is called a downstream TP in this paper. However, as shown in Fig. 5, we continued to increase k_R with reference to the basic case in Fig. 3. When $k_R = 2.0$, 3.0, and 4.0, the ODW first generates a sawtooth wave surface, as shown in Fig. 5(a), which means that a primary instability appears. Then, the more irregular keystone wave surface is generated at a position further downstream of the ODW, as shown in Fig. 5(b), which means that a secondary instability appears. The wave surface positions of both the primary and secondary instabilities have clearly moved upstream as the heat release rate k_R increases. This is also consistent with the findings in a previous study.[24] The transverse wave of the TP generated by the primary instability is essentially a left-traveling shock wave. The keystone wave surface generated by the secondary instability also includes a right-traveling transverse wave based on the left-traveling transverse wave. However, the TPs move downstream on the whole in the above cases. When k_R increases to 5.0, as shown in Fig. 5(d), a TP that propagates upstream on the whole is generated on the wave surface near the main TP, i.e., the transition point between the ODW and OSW. The upstream TP and downstream TP can be distinguished easily via numerical smoke trail diagrams, which will be introduced in detail in the next paragraph. It continuously propagates upstream and eventually merges with the main TP, which causes a small oscillation in the position of the main TP. However, this
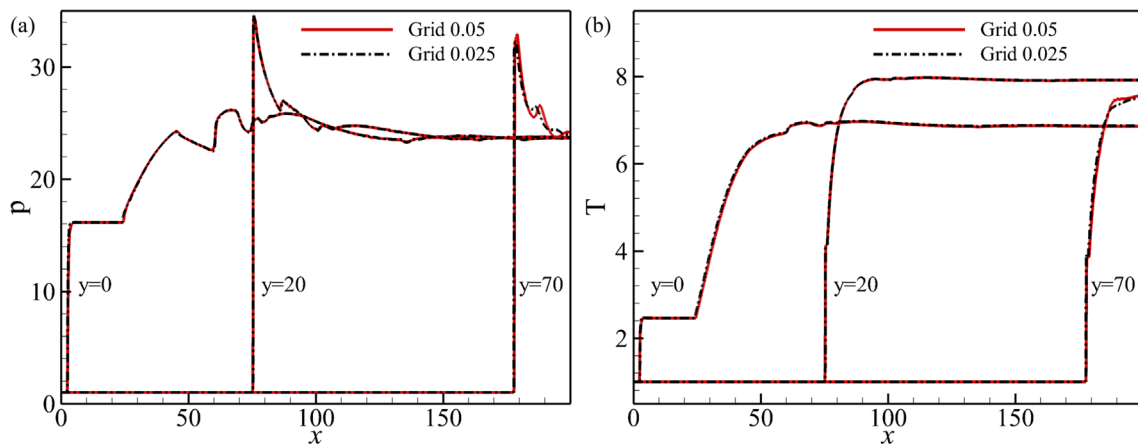

FIG. 4. Pressure profiles (a) and temperature profiles (b) along different lines parallel to the x-axis for the grid scales 0.05 and 0.025.
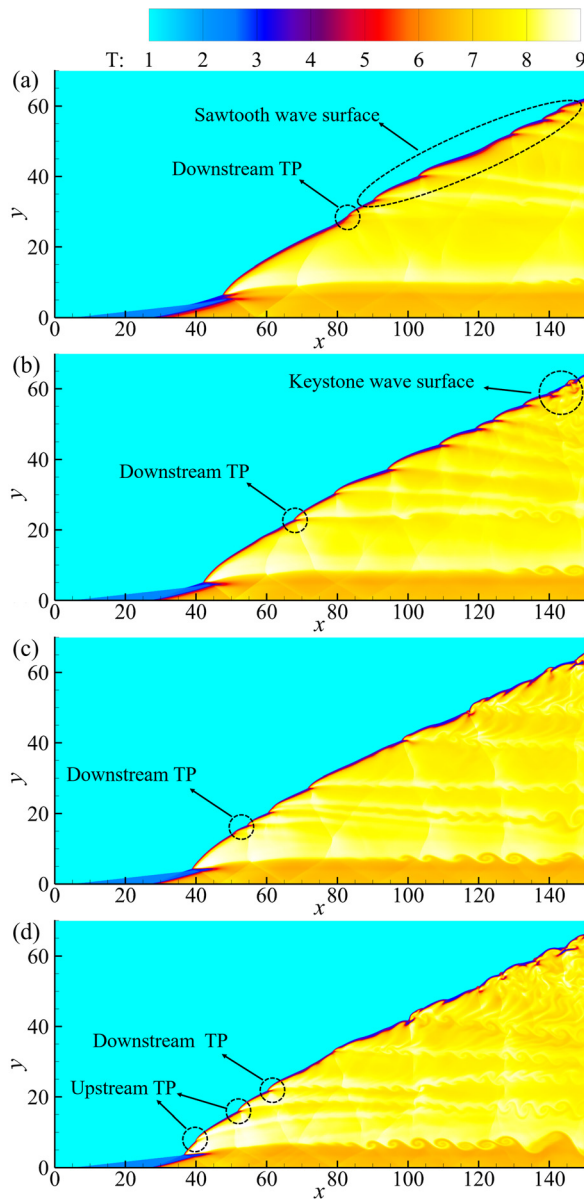
FIG. 5. Temperature fields for $M_0 = 6.5$, $\theta = 30°$, and $k_R = 2.0$ (a), 3.0 (b), 4.0 (c), and 5.0 (d).

FIG. 6. Smoked cells for $M_0 = 6.5$, $\theta = 30°$, and $k_R = 2.0$ (a), 3.0 (b), 4.0 (c), and 5.0 (d).

oscillation does not destabilize the overall structure of the ODW initiation zone. The results in Figs. 3 and 5 indicate qualitatively that increasing the heat release rate k_R makes the ODW surface more unstable and results in generation of upstream TPs.

The orange images in Fig. 6 are the numerical smoke trail diagrams corresponding to the parameters in Fig. 5. They are the trajectories formed by the maximum wave pressure at multiple moments in sequence and can better reflect the evolution process of the TPs. The right end represents the maximum wave pressure at the beginning of recorded moment, while the left end represents the maximum wave pressure at the ending of recorded 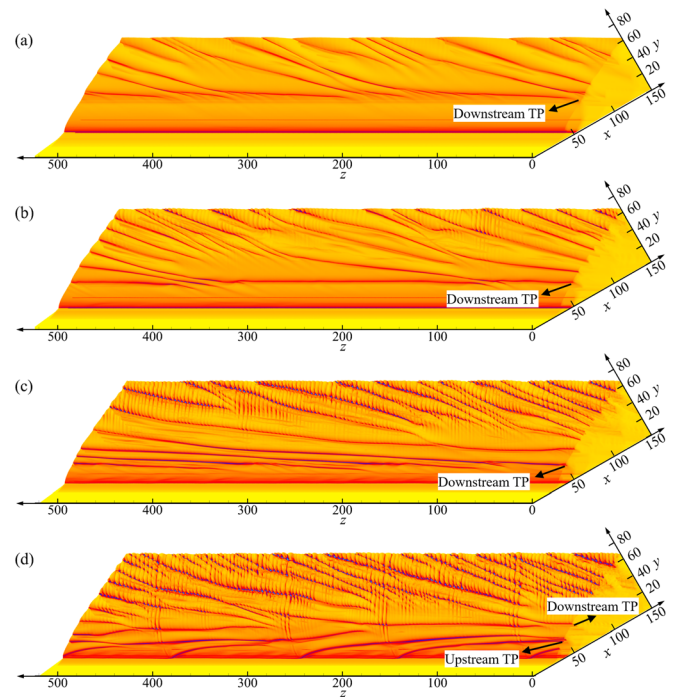moment. The distance between the left end and right end along the z-direction is the product of the inflow velocity U and the difference Δt between the ending and beginning recorded moments, i.e., $z = U \times \Delta t$. Because the inflow velocity is fixed, the z-direction can reflect the time characteristic. For x-direction and y-direction, they are consistent with that of the two-dimensional figures as shown in Figs. 5 and 7.

Figure 6 shows that the generation of an upstream TP is closely related to the forward movement of the primary instability on the wave surface. It is clearer from Figs. 6(a)–6(c) that as the heat release rate k_R increases, the positions of the primary and secondary instabilities on the wave surface indeed both move upstream. The slope of the TP trajectory decreases in the upstream direction of the wave surface, which means the speed of the TPs is slower. Figures 6(a)–6(c) show that the TPs closest to the upstream move slowly, but still propagate downstream eventually. When k_R increases further to 5.0 in Fig. 6(d), the TPs generated by the wave surface instability still propagate downstream when they are near the wave surface downstream, which is the same as in Figs. 6(a)–6(c). The difference is that an upstream TP that propagates oppositely to the aforementioned TPs is generated near the main TP. The upstream TP forms in the area of slower TPs near the upstream of the wave surface and then continues to propagate upstream until it merges with the main TP. The slope of the upstream TP trajectory increases in the process, which shows the speed of the upstream TP increases.

With reference to the basic case in Fig. 3, the angle of the wedge was increased from 30° to 35°. The results are shown in Fig. 7. The increase in wedge angle results in generation of steady TPs. The inclination angle of the ODW surface increases with the increasing wedge angle. As shown in Figs. 7(a) and 7(b), the wave surface instability
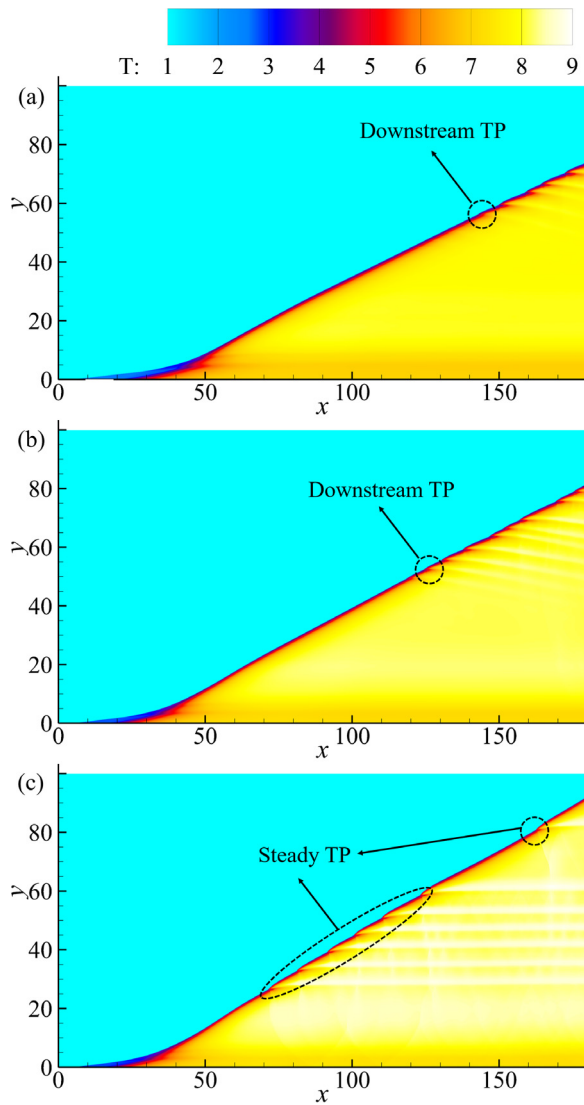
FIG. 7. Temperature fields for $M_0 = 6.5$, $k_R = 1.0$, and $\theta = 32°$ (a), 34° (b), and 35°(c).

position keeps moving upstream as the wedge angle increases, which is different from previous research results.[19] Generally speaking, the increase in the wedge angle will increase the overdrive degree of the ODW, which will increase its ability to resist instability. And the wave surface is less prone to instability, so the instability appears at a more downstream position. However, the results of our study show that when the wedge surface angle is relatively large and is constantly approaching the critical detachment angle, its instability position gradually moves forward. (When the incoming Mach number is 6.5, the critical detachment angle calculated from the detonation pole curve is about 35.5°.) When the wedge angle increases to 35°, TPs appear which stand on the wave surface, as shown in Fig. 7(c). This type of TP first moves upstream along the wave surface after it is generated and finally stands at a certain position. The motion of the steady TP is

obviously different from that of the TPs on the wave surface that were studied above. Figure 7(c) shows six steady TPs approximately equally spaced in the middle of the wave surface, and there is also a steady TP that is farther from the previous six steady TPs near the downstream.

The parameters of the numerical smoke trace diagrams in Fig. 8 correspond to those in Fig. 7, and their generation principle is consistent with Fig. 6. According to the definition of numerical smoke trace diagrams, the ratio of TPs moving distance to corresponding z-direction component (i.e., the slope of TPs trajectories relative to z-direction) can represent the moving speed of TPs. The smaller the slope, the slower the TPs move. Therefore, Fig. 8 shows that the moving speed of TPs generated by wave surface instability gradually decreases as the wedge angle increases. When the wedge angle increases to 32° and 34°, the TPs generated by the wave surface instability move downstream. The wave surface angle of the ODW also increases as the wedge angle increases. Meanwhile, the slope of the TP trajectory decreases, which indicates that the motion of the TPs
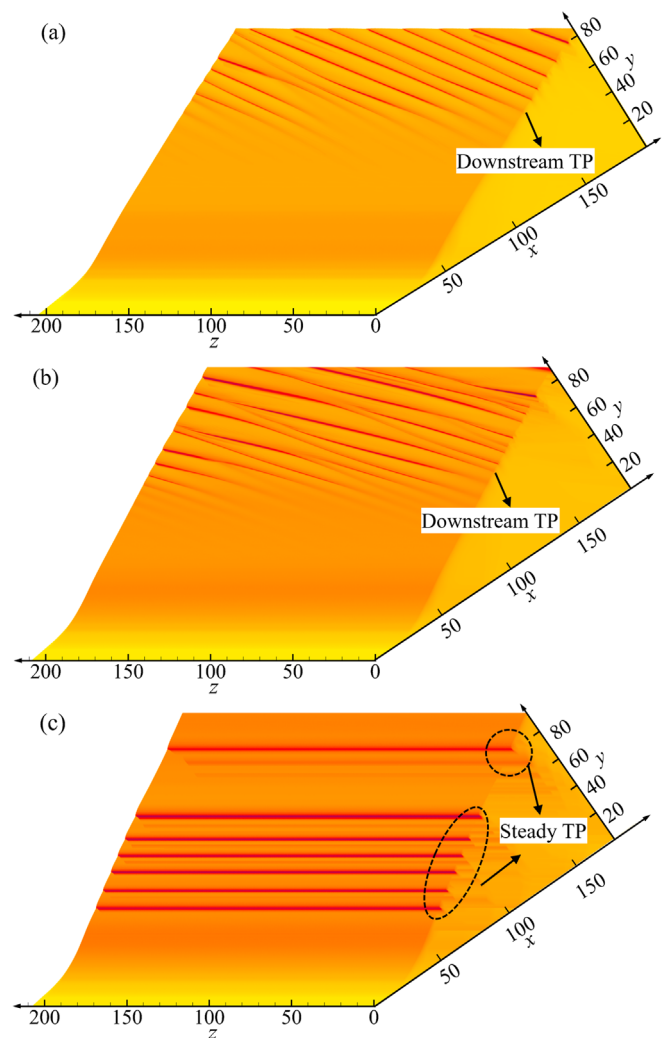

FIG. 8. Smoked cells for $M_0 = 6.5$, $k_R = 1.0$, and $\theta = 32°$ (a), 34° (b), and 35° (c).

becomes slower as the wave surface angle rises. Figure 8 also shows that the ODW wave surfaces in all three cases are sawtooth-shaped, which indicates that only the primary instability occurs on these wave surfaces in the current computing domain. The TP trajectories are relatively regular. A steady TP is generated when the wedge angle increases to 35°, as shown in Fig. 8(c). Its trajectory is a horizontal straight line, indicating that the position of this steady TP on the wave surface no longer changes with time.

The statistical results under different parameter values are shown in Table I. Upstream and steady TPs are observed at Mach numbers of 6.0 and 7.0 in addition to Mach 6.5, which indicates that the phenomenon described above is not an individual case. When certain parameter conditions are met, the ODW surface produces the corresponding type of TPs. Three general laws can be deduced. First, Table I shows that when the Mach number and wedge angle are constant, increasing k_R results in upstream TPs. Taking a Mach number of 7.0 and wedge angle of 34° as an example, the wave surface instability only produces downstream TPs when k_R is 5.0. When k_R increases to 8.0, an upstream TP is generated near the main TP. Note that for hydrogen and small hydrocarbon fuels such as acetylene, their chemical reaction is very violent. The large k_R can be acquired easily in the large pressure. Second, when the Mach number and k_R are constant and the wedge angle approaches the critical detachment angle, steady TPs are generated that stand on the wave surface. When the Mach number is 6.0, k_R is 0.45, and the wedge angle is 30°, the wave surface instability only produces downstream TPs. When the wedge angle increases to 31°, the wave surface instability produces steady TPs that propagate upstream first and then stand on the wave surface. Finally, when θ and k_R are fixed as constants, increasing the inflow Mach number leads to generation of downstream TPs. Taking a wedge angle of 30° and k_R value of 5.0 as an example, increasing the inflow Mach number from 6.5 to 7.0 causes the upstream TP to disappear, and the TPs generated by the wave surface instability all propagate downstream. The reason may be that increasing the incoming flow speed inhibits TP propagation upstream.

C. Mechanism of TP propagation

Previous studies[22,42–44] have shown that regardless of whether a transverse TP wave is generated on an NDW or ODW surface, it is essentially a weak shock wave with a propagation velocity slightly greater than the speed of sound. That is to say, a transverse wave generated by a primary instability on the ODW surface is a left-traveling weak shock wave. The strong transmission effect of the incoming flow generally causes it to be carried and propagate downstream. However, under certain parameter conditions, TPs are generated that can continuously propagate upstream and stand on the wave surface. On this basis, we first assume that the final propagation direction of TPs is determined by the relationship between the post-ODW flow speed and the transverse wave velocity.

To explain the propagation pattern of TPs in more detail, we quantified the post-ODW flow speed and the transverse wave velocity. In Fig. 9, the black solid line almost parallel to the wave surface is the half-reaction zone curve, where the exothermic reaction has progressed to 50%. Actually, whichever process variable value is chosen from 0% to 100%, the relationship between the post-ODW flow speed and the transverse wave velocity can be both acquired, which should conform to next our proposed criteria. As shown in Figs. 15–17 in Appendix B, when the location of the progress variable being 1% ($\approx$0%), the similar conclusion consistent with 50% progress variable can be drawn from the results. In addition, 50% progress variable can represent the average level of results to some extent. The black dashed line that is curved represents a transverse wave. This study characterized the transport velocity of the incoming flow using the normal component of the flow velocity perpendicular to the transverse wave before the intersection point of the transverse wave and the half-reaction curve. The formula is

$$U_\tau = \sqrt{u_1^2 + v_1^2} \sin \alpha, \qquad (11)$$

where u_1 and v_1 are the velocity components in the x and y directions before the intersection of the transverse wave and half-reaction curve, and α is the angle between the direction of the flow velocity before the intersection point and the transverse wave.

Because the transverse wave in the TP can be regarded as a weak shock wave, its own speed can be calculated from the relational formula for the motion of a shock wave,[45] which is

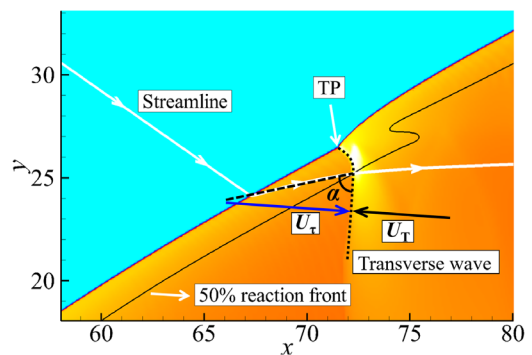$$U_T = \sqrt{\frac{1}{2\rho_1}[(\gamma - 1)p_1 + (\gamma + 1)p_2]}, \qquad (12)$$

TABLE I. TP type depending on various parameters.

M_0	θ (°)	k_R	Type of TP
6.0	30.0	0.45	Downstream
6.0	30.0	0.65	Upstream
6.0	31.0	0.45	Steady
6.5	30.0	1.0–4.0	Downstream
6.5	30.0	5.0	Upstream
6.5	31.0–34.0	1.0	Downstream
6.5	35.0	1.0	Steady
7.0	30.0	1.0–8.0	Downstream
7.0	34.0	1.0–5.0	Downstream
7.0	34.0	8.0–10.0	Upstream
7.0	38.0	1.9	Steady

FIG. 9. Diagram of an ODW local front with TPs.

where ρ_1 and p_1 are the density and pressure before the intersection of the transverse wave and the half-reaction curve, and p_2 is the pressure after the intersection. The detailed derivation process on Eq. (12) is shown in the Appendix C.

Using the above method, we first calculated the situation in which the wave surface instability only produces downstream TPs. The values of U_τ and U_T in Fig. 10 are calculated for an incoming flow Mach number of 6.5, k_R value of 1.0, and wedge surface angles of 32° and 34°. The solid line represents U_τ, and the dotted line represents U_T. Three different moments are selected. At each moment, five TPs on the wave surface are selected to calculate U_τ and U_T. The value of U_τ in Fig. 10(a) fluctuates at approximately 4, and the amplitude of the fluctuation is small. U_T is concentrated near 3. The distributions of U_τ and U_T in Fig. 10(b) are not as concentrated as in Fig. 10(a) and are more scattered. The fluctuation amplitude of U_τ obviously corresponds to different TPs at the same moment. This characteristic can also be seen from the corresponding numerical smoke traces in Figs. 8(a) and 8(b). The trajectory of the TPs in Fig. 8(b) is more irregular than that in Fig. 8(a) because of the increase in wedge angle. What Figs. 10(a) and 10(b) obviously have in common is that U_τ is higher than U_T, which indicates the forward speed of the TPs is not enough to resist the transport speed of the incoming flow. Therefore, the TPs have an overall tendency to be carried downstream by the incoming flow.

The variational tendencies of U_τ and U_T in Fig. 11 are obviously different, which results in different movement patterns between upstream TPs and steady TPs. The plots in Fig. 11(a) show the evolution of U_τ and U_T for a TP that propagates upstream continuously and periodically, while the plots in Fig. 11(b) show the evolution of U_τ and U_T for a steady TP that propagates upstream first and then stands on the wave surface. The duration chosen in Fig. 11 is a complete period from TP formation to ending. When the continuously upstream TP in Fig. 11(a) is just formed, U_T represented by the dotted line is greater than U_τ represented by the solid line, so the TP first travels upstream. During the upstream propagation, U_T is basically unchanged while U_τ significantly declines over time. This causes the gap between U_T and U_τ to increase, so the TP propagates upstream continuously. Finally, it collides and merges with the main TP. Figure 11(b) records the process from the formation of the first steady TP on the wave surface to the final stationary TP. When the TP first forms, its U_T is greater than U_τ, so it also propagates upstream first. Unlike the situation in Fig. 11(a), the gap between them decreases with time although both U_T and U_τ increase slightly at the beginning. Finally, U_T and U_τ tend to be almost the same and achieve a balance, so the TPs can stand on the wave surface.

To further analyze the propagation mechanism of the TPs in the above two cases, we studied the pressure field around the TP. The results in Figs. 12(a) and 12(b) correspond to the local pressure flow field around the upstream TP and steady TP, respectively. The plots in Figs. 12(c) and 12(d) are for the inclination angle β of the local wave surface as the TP trace moves forward. The closer the TP in Fig. 12(a) is to the upstream, the greater the inclination of the wave surface is, as shown in Fig. 12(c), and the tangential transport effect of the incoming
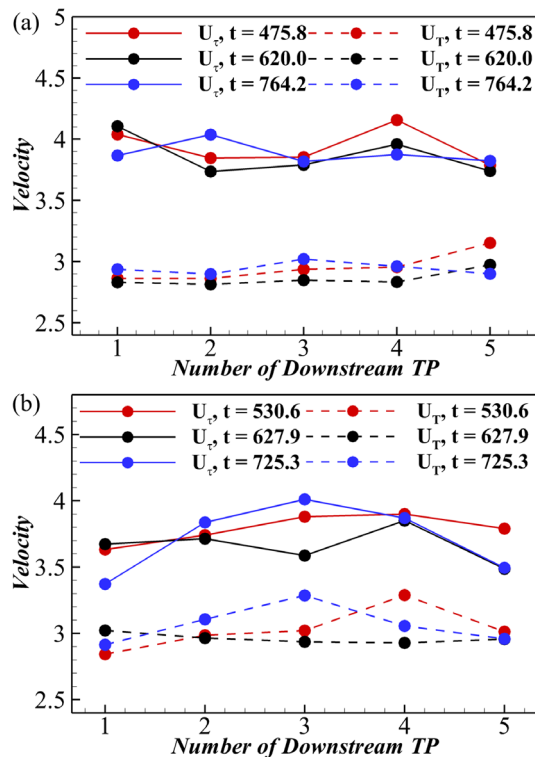

FIG. 10. Downstream TP velocity and inflow tangential velocity before downstream TPs at different moments for $M_0 = 6.5$, $k_R = 1.0$, and $\theta = 32°$ (a) and 34° (b).
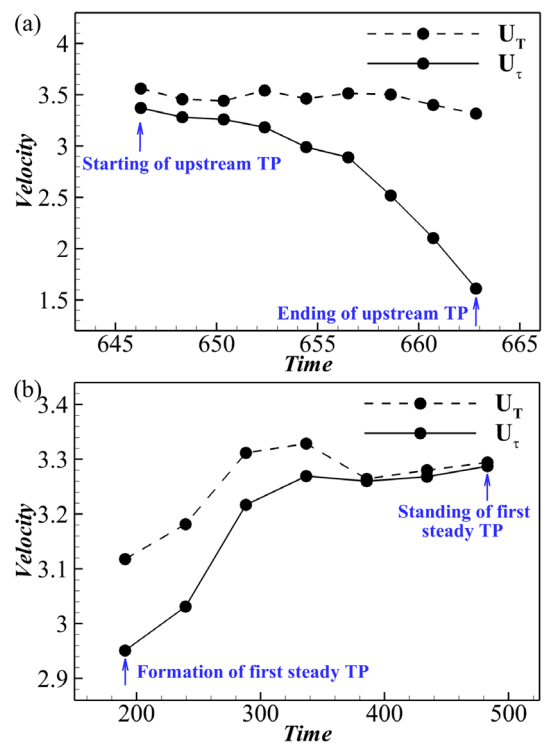

FIG. 11. U_T and U_τ for an upstream TP with $M_0 = 6.5$, $k_R = 5.0$, and $\theta = 30°$ (a); U_T and U_τ for a steady TP with $M_0 = 6.5$, $k_R = 1.0$, and $\theta = 35°$ (b).
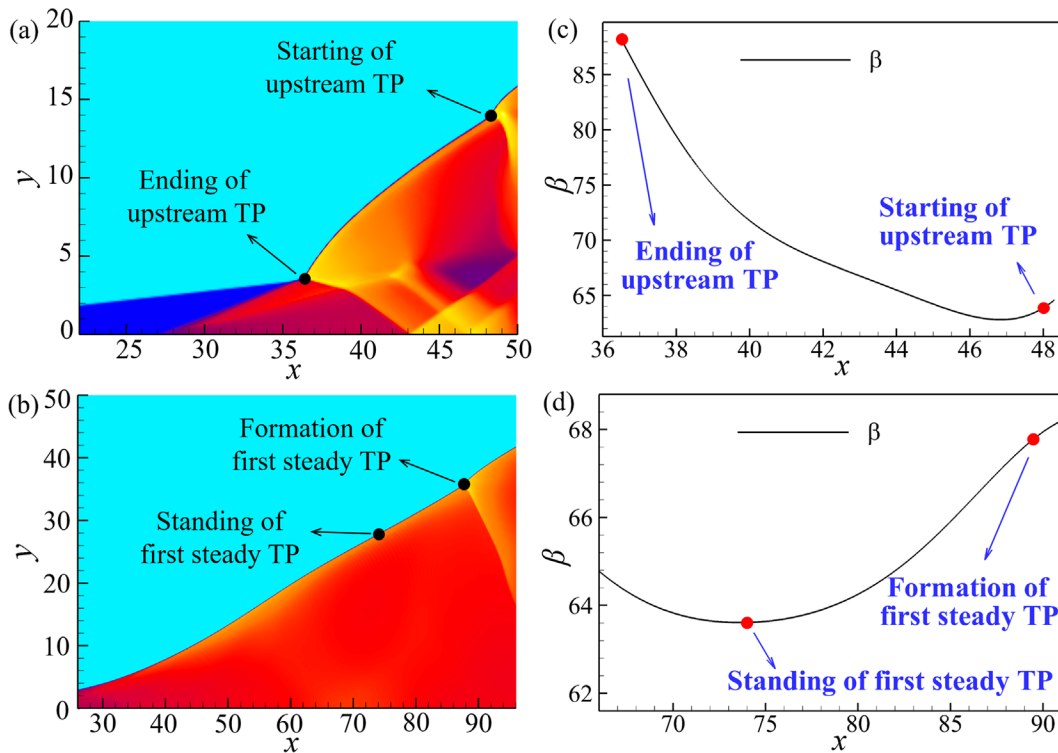
FIG. 12. Pressure fields of a local zone near TPs for $M_0 = 6.5$, $k_R = 5.0$, and $\theta = 30°$ (a); $M_0 = 6.5$, $k_R = 1.0$, and $\theta = 35°$ (b); inclination angle of local wave surface for $M_0 = 6.5$, $k_R = 5.0$, and $\theta = 30°$ (c); $M_0 = 6.5$, $k_R = 1.0$, and $\theta = 35°$ (d).

flow gradually weakens. That is, the ability of the incoming flow to resist the forward motion of the TP weakens, which corresponds to the time-varying plot of U_τ in Fig. 11(a). Therefore, the TP propagates upstream continuously. As for the TP that eventually stands on the wave surface, Fig. 12(b) shows that the inclination angle β of the wave surface also changes in a local area. Although the change in angle is not as obvious as in Fig. 12(a), it is also visible to the naked eye and shown in Fig. 12(d) clearly. The first steady TP on the wave surface

forms at approximately $x = 88$ and stands on the wave surface at approximately $x = 74$. The inclination of the wave surface gradually decreases from the formation to the upstream propagation of the steady TP, which causes the tangential transmission function of the incoming flow to gradually increase. That is, the incoming flow's resistance to the forward TP motion is enhanced. Finally, the flow resistance is enough to make the TP stationary on the wave surface. This is contrary to the situation in Fig. 12(a) and corresponds to the plot of U_τ over time in Fig. 11(b).

Figure 13 shows U_τ and U_T at three different moments after the six TPs on the wave surface are all stationary. Two conclusions can be drawn from the results. On the one hand, U_τ and U_T for the same TP hardly change in any of the three moments, which indicates that the TP has indeed stabilized on the wave surface. On the other hand, the U_τ and U_T values of the six TPs on the wave surface tend to be the same at the same moment, and the maximum difference does not exceed 0.04. This shows that the first steady TP discussed above is not an exception. The essential reason that the TPs can stand on the wave surface is that U_τ and U_T have reached a matching balance.
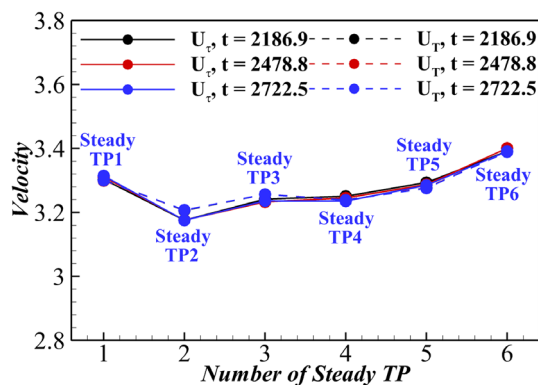

FIG. 13. Steady TP velocity and inflow tangential velocity before steady TPs at different times for $M_0 = 6.5$, $k_R = 1.0$, and $\theta = 35°$.

IV. CONCLUSIONS

Many studies[14–19] have focused on the evolution of downstream TPs, while knowledge on upstream and steady TPs has been lacking. This study used the reactive Euler equations with a two-step induction–reaction kinetic model to simulate oblique detonations and analyze different types of TP motion.

The TPs generated by ODW surface instabilities were divided into downstream, upstream, and steady TPs according to their propagation directions relative to the wedge. Two flow parameters were introduced to explain the formations of different types of TPs: the post-ODW flow speed U_τ and transverse wave velocity U_T. The ratio U_τ/U_T was used to predict the type of TP motion. When U_τ/U_T is approximately equal to 1, the TPs stand on the wave surface; when it is greater than 1, downstream TPs form, and when it is less than 1, upstream TPs form. Downstream, upstream, and steady TPs were obtained under different incoming Mach numbers by adjusting the wedge angle and chemical reaction rate. The criteria were further verified by quantitative analysis. A high chemical reaction rate is more conducive to formation of upstream TPs, while steady TPs mostly occur when the wedge angle approaches the detachment value. We also found that U_T remains almost unchanged during TP propagation, but U_τ changes dramatically. The reason is that U_τ is determined by the angle of the ODW surface, which is sensitive to different inflow parameters.

AUTHOR DECLARATIONS
Conflict of Interest

The authors have no conflicts to disclose.

DATA AVAILABILITY

The data that support the findings of this study are available from the corresponding author upon reasonable request.

APPENDIX A: THE VALIDATION OF HOMEMADE CODE

Following the fluid conservation laws, the oblique detonation wave angle β_D is determined by the wedge angle θ, amount of chemical heat release Q, and the inflow Mach number M_0,

$$\frac{\tan \beta_D}{\tan (\beta_D - \theta)} = \frac{(\gamma+1)M_0^2 \sin^2 \beta_D}{\gamma M_0^2 \sin^2 \beta_D + 1 \pm \sqrt{\left(M_0^2 \sin^2 \beta_D - 1\right)^2 - 2(\gamma^2 - 1)M_0^2 \sin^2 \beta_D \cdot Q}}. \tag{A1}$$

The variables have been referred in the text. Solving the above equation, β_D-–θ relation can be plotted as the detonation polar. The detonation polar curves based on the parameters, i.e., $Q = 50$, $\gamma = 1.2$, and $M_0 = 8$ and 10, are shown in Fig. 14. The solid line is the theoretical value, and the data points are the results of numerical simulation. From Fig. 14, the theoretical and numerical results are basically in agreement, indicating the accuracy of the homemade code.

The comparison of theoretical and numerical results mentioned above is mainly used to illustrate the accuracy of the final steady-state parameters of detonation combustion in numerical calculation, without considering the chemical reaction process. When the chemical reaction rate is finite, the oblique detonation wave induced by wedge can be divided into oblique shock wave, initiation zone, and oblique detonation wave, as shown in Fig. 2.

In order to verify the accuracy of the calculation program used in this paper, a set of chemical reaction parameters were given: $Q = 50$, $\gamma = 1.2$, $E_I = 5.0 T_S$, $E_R = 1.0 T_S$, and $k_R = 1.0$, and the theoretical and numerical results of the initiation zone length of oblique detonation wave under different inflow Mach numbers and wedge angles were compared. It can be seen from the comparison results in Table II that the numerical and theoretical results are basically consistent, and the program can accurately calculate the detonation wave related to the two-step reaction model.

APPENDIX B: CRITERION VALIDATION FOR OTHER REACTION PROCESS VARIABLE

As shown in Figs. 15–17, the results are carried out for the location of the progress variable being 1% ($\approx$0%) along the transverse
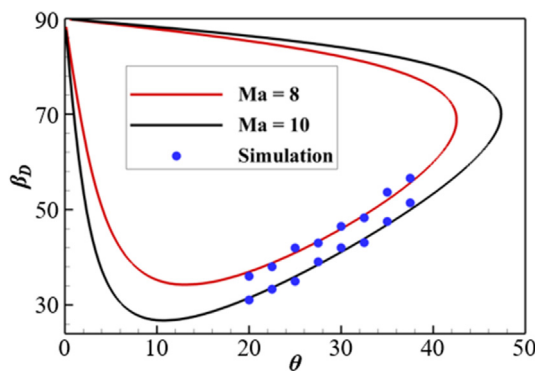

FIG. 14. Polar of oblique detonation wave: wave angle.

TABLE II. Induction length of wedge-induced oblique detonation wave for theoretical and numerical methods.

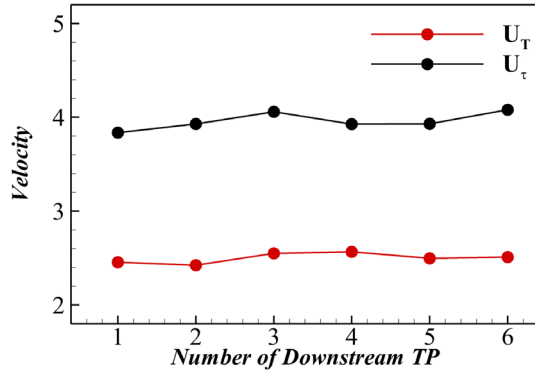| Theoretical/numerical	$Ma = 9.0$	$Ma = 10.0$	$Ma = 12.0$
$\theta = 25°$	283.6/282.2	114.6/113.9	27.8/28.0
$\theta = 28°$	98.8/98.2	42.5/42.3	11.8/11.6
$\theta = 30°$	53.7/52.8	24.2/24.0	7.4/7.4
$\theta = 32°$	31.2/30.6	14.7/14.5	4.8/4.7
$\theta = 35°$	15.3/15.1	7.7/7.6	2.8/2.8

FIG. 15. Downstream TP velocity and inflow tangential velocity before downstream TPs for $M_0 = 6.5$, $k_R = 1.0$, and $\theta = 32°$.
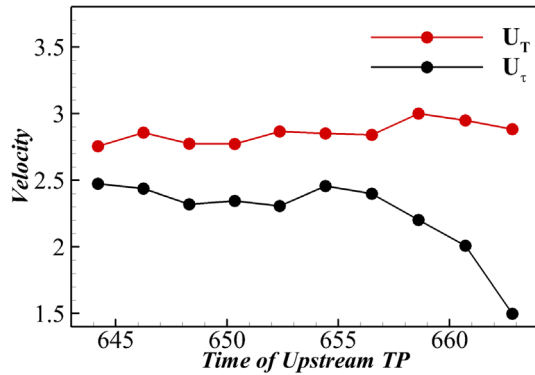

FIG. 16. Upstream TP velocity and inflow tangential velocity before upstream TPs at different times for $M_0 = 6.5$, $k_R = 5.0$, and $\theta = 30°$.

wave. It is clear that when U_τ/U_T is approximately equal to 1, the TPs stand on the wave surface; when it is greater than 1, downstream TPs form, and when it is less than 1, upstream TPs form. This is in accord with the progress variable being 50%.
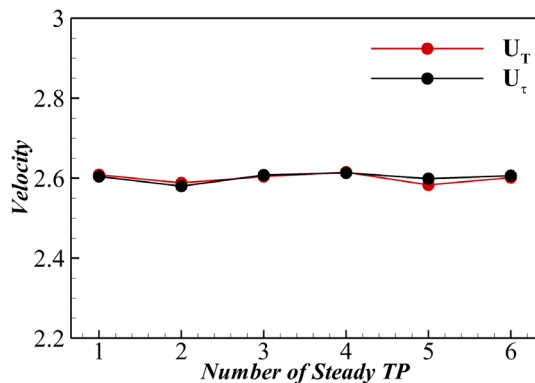

FIG. 17. Steady TP velocity and inflow tangential velocity before steady TPs for $M_0 = 6.5$, $k_R = 1.0$, and $\theta = 35°$.
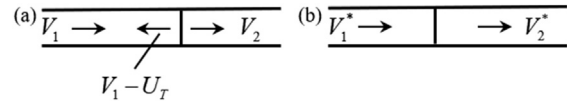

FIG. 18. The left-traveling shock wave in laboratory coordinates (a) and shock coordinates (b).

APPENDIX C: DERIVATION OF MOVING SHOCK WAVE RELATION

In Sec. III C, we have illuminated that a transverse wave generated by a primary instability on the ODW surface is a left-traveling weak shock wave, that is, the transverse wave's own velocity is opposite to that of the inflow. Therefore, the relation of transverse wave velocity and inflow velocity can be described as follows:

The left-traveling shock wave in laboratory coordinates and shock coordinates is shown in Fig. 18. In laboratory coordinates, the velocity of shock wave is V_1-U_T. In the shock coordinates, the before-shock velocity V_1^* and post-shock velocity V_2^* are U_T and U_T-$V_1 + V_2$, respectively. And mass conservation equation and momentum conservation equation can be written as follows:

$$m_A = \rho_1 V_1^* = \rho_2 V_2^*, \tag{C1}$$

$$p_1 + \rho_1 V_1^{*2} = p_2 + \rho_2 V_2^{*2}. \tag{C2}$$

Combining Eq. (C1) and Eq. (C2), Eq. (C3) can be derived,

$$p_2 - p_1 = m_A^2 \left(\frac{1}{\rho_1} - \frac{1}{\rho_2} \right). \tag{C3}$$

Combining Eq. (C3) and the Rankine-Hugoniot relationship, i.e., Eq. (C4), eliminating ρ_2, Eq. (C5) can be derived,

$$\frac{\rho_2}{\rho_1} = \left(\frac{\gamma + 1}{\gamma - 1} \frac{p_2}{p_1} + 1 \right) \bigg/ \left(\frac{\gamma + 1}{\gamma - 1} + \frac{p_2}{p_1} \right), \tag{C4}$$

$$m_A^2 = \rho_1^2 V_1^{*2} = \frac{\rho_1}{2} [(\gamma - 1)p_1 + (\gamma + 1)p_2]. \tag{C5}$$

Therefore, Eq. (C6) is finally derived,

$$U_T = V_1^* = \sqrt{\frac{1}{2\rho_1}[(\gamma - 1)p_1 + (\gamma + 1)p_2]}. \tag{C6}$$

REFERENCES

[1] P. Wolański, "Detonative propulsion," Proc. Combust. Inst. **34**, 125–158 (2013).
[2] V. Anand and E. Gutmark, "Rotating detonation combustors and their similarities to rocket instabilities," Prog. Energy Combust. Sci. **73**, 182–234 (2019).
[3] K. Kailasanath, "Recent developments in the research on pulse detonation engines," AIAA J. **41**, 145–159 (2003).
[4] Z. Jiang, Z. Zhang, Y. Liu, C. Wang, and C. Luo, "Criteria for hypersonic air-breathing propulsion and its experimental verification," Chin. J. Aeronaut. **34**, 94–104 (2021).
[5] J. Koch, M. Kurosaka, C. Knowlen, and J. N. Kutz, "Mode-locked rotating detonation waves: Experiments and a model equation," Phys. Rev. E **101**, 013106 (2020).
[6] J. Koch and J. N. Kutz, "Modeling thermodynamic trends of rotating detonation engines," Phys. Fluids **32**, 126102 (2020).
[7] G. J. Sharpe, "Transverse waves in numerical simulations of cellular detonations," J. Fluid Mech. **447**, 31–51 (2001).

[8]R. A. Strehlow and F. D. Fernandes, "Transverse waves in detonations," Combust. Flame **9**, 109–119 (1965).

[9]B. Zhang, X. Shen, L. Pang, and Y. Gao, "Detonation velocity deficits of H_2/O_2/Ar mixture in round tube and annular channels," Int. J. Hydrogen Energy **40**, 15078–15087 (2015).

[10]Q. Xiao and C. Weng, "Effect of losses on hydrogen–oxygen–argon detonation cell sizes," Phys. Fluids **33**, 116103 (2021).

[11]B. Zhang, H. Liu, B. Yan, and H. D. Ng, "Experimental study of detonation limits in methane-oxygen mixtures: Determining tube scale and initial pressure effects," Fuel **259**, 116220 (2020).

[12]M. V. Papalexandris, "A numerical study of wedge-induced detonations," Combust. Flame **120**, 526–538 (2000).

[13]C. Viguier, A. Gourara, and D. Desbordes, "Three-dimensional structure of stabilization of oblique detonation wave in hypersonic flow," Symp. (Int.) Combust. **27**, 2207–2214 (1998).

[14]J. Y. Choi, D. W. Kim, I. S. Jeung, F. Ma, and V. Yang, "Cell-like structure of unstable oblique detonation wave from high-resolution numerical simulation," Proc. Combust. Inst. **31**, 2473–2480 (2007).

[15]M. Y. Gui, B. C. Fan, and G. Dong, "Periodic oscillation and fine structure of wedge-induced oblique detonation waves," Acta Mech. Sin. **27**, 922–928 (2011).

[16]H. H. Teng, Z. L. Jiang, and H. D. Ng, "Numerical study on unstable surfaces of oblique detonations," J. Fluid Mech. **744**, 111–128 (2014).

[17]Y. Zhang, L. Zhou, J. Gong, H. D. Ng, and H. Teng, "Effects of activation energy on the instability of oblique detonation surfaces with a one-step chemistry model," Phys. Fluids **30**, 106110 (2018).

[18]H. Teng, H. D. Ng, K. Li, C. Luo, and Z. Jiang, "Evolution of cellular structures on oblique detonation surfaces," Combust. Flame **162**, 470–477 (2015).

[19]J. Verreault, A. J. Higgins, and R. A. Stowe, "Formation of transverse waves in oblique detonations," Proc. Combust. Inst. **34**, 1913–1920 (2013).

[20]H. Guo, X. Jia, N. Zhao, S. Li, H. Zheng, C. Sun, and X. Chen, "The formation and development of oblique detonation wave with different chemical reaction models," Aerosp. Sci. Technol. **117**, 106964 (2021).

[21]Y. Huang, Z. Luan, Z. Li, H. Ji, and Y. You, "Study on the flow characteristics in the non-detonation reaction zones of wedge-induced oblique detonation transitions," Aerosp. Sci. Technol. **120**, 107282 (2022).

[22]J. Y. Choi, E. J. R. Shin, D. R. Cho, I. S. Jeung, and V. Yang, "Onset condition of oblique detonation wave cell structures," in 46th AIAA Aerospace Sciences Meeting and Exhibit, Reno, Nevada, 7–10 January, 2008.

[23]Y. Liu, B. Xiao, L. Wang, and C. Wang, "Numerical study of disturbance resistance of oblique detonation waves," Int. J. Aerospace Eng. **2020**, 1–9.

[24]P. Yang, H. Teng, H. D. Ng, and Z. Jiang, "A numerical study on the instability of oblique detonation waves with a two-step induction–reaction kinetic model," Proc. Combust. Inst. **37**, 3537–3544 (2019).

[25]H. Guo, H. Yang, N. Zhao, S. Li, and H. Zheng, "Influence of incoming flow velocity and mixture equivalence ratio on oblique detonation characteristics," Aerosp. Sci. Technol. **119**, 107088 (2021).

[26]H. Teng, Y. Zhang, P. Yang, and Z. Jiang, "Oblique detonation wave triggered by a double wedge in hypersonic flow," Chin. J. Aeronaut. **35**, 176–184 (2022).

[27]K. C. Uy, L. Shi, and C. Wen, "Chemical reaction mechanism related vibrational nonequilibrium effect on the Zel'dovich−von Neumann−Döring (ZND) detonation model," Combust. Flame **196**, 174–181 (2018).

[28]G. Xiang, Y. Zhang, X. Gao, H. Li, and X. Huang, "Oblique detonation waves induced by two symmetrical wedges in hydrogen-air mixtures," Fuel **295**, 120615 (2021).

[29]G. X. Xiang, X. Gao, W. J. Tang, X. Z. Xie, and X. Huang, "Numerical study on transition structures of oblique detonations with expansion wave from finite-length cowl," Phys. Fluids **32**, 056108 (2020).

[30]S. Taileb, J. Melguizo-Gavilanes, and A. Chinnayya, "The influence of the equation of state on the cellular structure of gaseous detonations," Phys. Fluids **33**, 036105 (2021).

[31]H. D. Ng, M. I. Radulescu, A. J. Higgins, N. Nikiforakis, and J. H. S. Lee, "Numerical investigation of the instability for one-dimensional Chapman–Jouguet detonations with chain-branching kinetics," Combust. Theory Model. **9**, 385–401 (2005).

[32]P. Yang, H. D. Ng, and H. Teng, "Numerical study of wedge-induced oblique detonations in unsteady flow," J. Fluid Mech. **876**, 264–287 (2019).

[33]X. Q. Yuan, C. Yan, J. Zhou, and H. D. Ng, "Computational study of gaseous cellular detonation diffraction and re-initiation by small obstacle induced perturbations," Phys. Fluids **33**, 047115 (2021).

[34]H. Teng, H. D. Ng, P. Yang, and K. Wang, "Near-field relaxation subsequent to the onset of oblique detonations with a two-step kinetic model," Phys. Fluids **33**, 096106 (2021).

[35]Z. Ren and B. Wang, "Numerical study on stabilization of wedge-induced oblique detonation waves in premixing kerosene-air mixtures," Aerosp. Sci. Technol. **107**, 106245 (2020).

[36]P. Yang, H. Teng, Z. Jiang, and H. D. Ng, "Effects of inflow Mach number on oblique detonation initiation with a two-step induction-reaction kinetic model," Combust. Flame **193**, 246–256 (2018).

[37]Z. Jiang, "On dispersion-controlled principles for non-oscillatory shock-capturing schemes," Acta Mech. Sin. **20**, 1–15 (2004).

[38]H. H. Teng and Z. L. Jiang, "On the transition pattern of the oblique detonation structure," J. Fluid Mech. **713**, 659–669 (2012).

[39]W. Han, C. Wang, and C. K. Law, "Three-dimensional simulation of oblique detonation waves attached to cone," Phys. Rev. Fluid **4**, 053201 (2019).

[40]Y. Zhang, Y. Fang, H. D. Ng, and H. Teng, "Numerical investigation on the initiation of oblique detonation waves in stoichiometric acetylene–oxygen mixtures with high argon dilution," Combust. Flame **204**, 391–396 (2019).

[41]G. Q. Zhang, S. F. Gao, and G. X. Xiang, "Study on initiation mode of oblique detonation induced by a finite wedge," Phys. Fluids **33**, 016102 (2021).

[42]J. J. Erpenbeck, "Nonlinear theory of unstable two-dimensional detonation," Phys. Fluids **13**, 2007–2026 (1970).

[43]J. Buckmaster, "Pressure transients and the genesis of transverse shocks in unstable detonations," Combust. Sci. Technol. **61**, 1–20 (1988).

[44]S. D. Watt and G. J. Sharpe, "Linear and nonlinear dynamics of cylindrically and spherically expanding detonation waves," J. Fluid Mech. **522**, 329–356 (2005).

[45]Z. Han and X. Yin, *Shock Dynamics* (Springer Science & Business Media, New York, 2013).